Smoothed particle hydrodynamics modeling of electrodeposition and dendritic growth under migration- and diffusion-controlled mass transport

Andrew Cannon¹, J. Gregory McDaniel¹, Emily Ryan^{1,2,3,*}

- 1. Department of Mechanical Engineering, Boston University, Boston, MA
- 2. Division of Materials Science and Engineering, Boston University, Boston, MA
- 3. Institute for Global Sustainability, Boston University, Boston, MA

Abstract

In many electrochemical processes, the transport of charged species is governed by the Nernst-Planck equation, which includes terms for both diffusion and electrochemical migration. In this work, a multiphysics, multi-species model based on the smoothed particle hydrodynamics (SPH) method is presented to model the Nernst-Planck equation in systems with electrodeposition. Electrodeposition occurs when ions are deposited onto an electrode. These deposits create complex boundary geometries, which can be challenging for numerical methods to resolve. SPH is a particularly effective numerical method for systems with moving and deforming boundaries due to its particle nature. This paper discusses the SPH implementation of the Nernst-Planck equations with electrodeposition and verifies the model with an analytical solution and a numerical integrator. A convergence study of migration and precipitation is presented to illustrate the model's accuracy, along with comparisons of the deposition growth front to experimental results.

Keywords: Electrochemical deposition, dendrite growth, mass transport, smoothed particle hydrodynamics

Introduction

Electrochemical systems are ubiquitous, found in everything from commercial electronics to alternative fuel vehicles. In electrochemical processes, mass transport and surface reactions are driven by complex, coupled phenomena at the interfaces, such as electrodeposition[1]. Electrodeposition is the deposition of metallic ions (disassociated in an electrolyte) onto an electrically conductive surface (the electrode) in the presence of an electric field[2,3]. This process is used to plate materials such as automobile parts and beverage containers[4,5] or to create thin metallic films for devices such as fuel cells and water splitting[6,7], and also describes the process of charging lithium metal batteries (LMB)[8–11].

One of the primary challenges associated with the electrodeposition process is non-uniform deposition and subsequent dendritic growth. Control over dendrite morphology is an important aspect of industrial processes[12]. Additionally, dendritic growth can cause safety and performance issues in LMBs[8,10,13]. Experimentally observing the electrodeposition process and dendrite morphology *in situ* at an interface is challenging due to its embedded nature and small scale. Alternatively, computational fluid dynamics (CFD) methods can isolate this region and study the critical physics and driving forces at the interface during electrodeposition[14,15].

Modeling geometrically and physically complex and moving reactive boundaries, i.e. non-uniform deposition or dendritic growth, can be challenging for CFD methods, especially in mesh-based methods.

^{*}Corresponding author: ryanem@bu.edu, 617-353-7767

The interfacial region is difficult to continuously track and the mesh must be updated at each time step leading to computationally inefficient models[16]. Moreover, the predictions of complex structures, such as dendrites, in mesh-based methods struggle to capture experimental data. These challenges make mesh-based CFD methods less than ideal for modeling electrodeposition.

To simplify modeling, some approaches assume that the concentration of charged species is constant at the interface[11,17]. However, fluctuations of ionic transport, which occur when the ionic concentration varies spatially and temporally[18], are the primary cause of non-uniform deposition [19]. Tracking the ionic concentration variation at the interface can enable greater understanding of the causes of non-uniform deposition. Recent computational modeling has focused on alternative methods such as Lagrangian methods, diffusion limited aggregation, and phase field methods (PFM). PFM has received the most attention in recent years, however, PFM has struggled to accurately capture the dendrite morphology and produces artificial symmetries and morphologies without modifications[20–22]. Chen et al.[23] have made improvements to the PFM modeling of dendrite growth by using a rate modification factor. Also, it is challenging to model complex structures in the diffusion region surrounding the anode with PFM, such as separator microstructures or anode protective layers. PFM also requires an additional differential equation (the phase-field equation) to resolve the interface which increases computational time.

In this study, we present a mesh-free model of the electrode-electrolyte interface for the study of electrodeposition based on smoothed particle hydrodynamics (SPH). The SPH method provides inherent solutions to many of the challenges of electrodeposition modeling [24]. SPH is a mesh-free, Lagrangian particle method that uses an interpolation scheme to solve the governing partial differential equations (PDE). The PDE's can be solved explicitly and exactly which simplifies their implementation. SPH conserves mass and does not need to explicitly track interfaces so that complex geometric structures, such as dendrites, can be handled without undue computational resources[25].

The model presented in this work builds upon a previous SPH model of diffusion and reactive interfaces with precipitation[26–29]. As discussed in the following sections, two main additions to the model have been included that enable more robust modeling of the electrodeposition process: (1) calculation of the spatially and temporally varying electric field, which is dependent on the local ionic concentrations, and (2) electrochemical migration mass transport. These additional physics allow the model to represent the electrodeposition process more accurately at the electrode-electrolyte interface. The implementation of the model is verified through comparison to an analytical solution and a numerical integrator. A convergence study of ionic migration and deposition growth front is presented. Finally, a qualitative validation of dendrite morphology is presented in comparison to experimental results for three operating conditions: high reaction rate, low reaction rate and pulse plating.

Governing Equations

The model solves for the mass and species conservation near the electrode-electrolyte interface, including the effects of an electric field, ionic diffusion-migration, and electrodeposition. The model assumes no convection, and dilute solution theory. The ion concentration at location $\overrightarrow{r_f}$ in the electrolyte, Ω_f , is governed by the Nernst-Planck equation, which includes mass transport mechanisms by both diffusion and migration[18],

$$\frac{\partial C_i(\overrightarrow{r_f},t)}{\partial t} = \nabla \cdot \left(D_i \nabla C_i(\overrightarrow{r_f},t) \right) + \mu_i \nabla \cdot \left(C_i(\overrightarrow{r_f},t) \nabla \phi(\overrightarrow{r_f},t) \right), \overrightarrow{r_f} \in \Omega_f, t > 0, \tag{1}$$

where C_i is the concentration of species i, D_i is the diffusion coefficient of species i, μ_i is the migration mobility coefficient of species i, and ϕ is the potential.

In a binary electrolyte, the two oppositely charged ions, denoted with subscripts a and c for anions and cations respectively, are dissolved in the electrolyte solution and remain electrically neutral[1]. If an electric potential is applied to the solution, the cations migrate toward the negatively charged electrode and the anions migrate away from the negatively charged electrode. As a result, the electric potential is altered by the charge disparity in the solution. The electric potential distribution is governed by the electrostatic Poisson equation [1],

$$\nabla^2 \phi(\overrightarrow{r_f}, t) = -\frac{\rho_e}{\epsilon}, \overrightarrow{r_f} \in \Omega_f, t > 0, \tag{2}$$

where ρ_e is the electric charge density given by

$$\rho_e = e(z_a C_a - z_c C_c),$$

e is the elementary charge, z_c and z_a are the cation and anion electric charge, and ϵ is the permittivity constant of the electrolyte. Note that in this form of Eq. 2, the permittivity constant of the electrolyte is assumed to be spatially independent.

During electrodeposition, cations (M⁺) are reduced at the electrode/dendrite surface,

$$M^+ + e^- \to M. \tag{3}$$

This reaction is controlled by the reaction rate, k, and the ionic concentration at the electrode-electrolyte interface, Γ . The reduction reaction rate is mainly controlled by the operating conditions of the process, although secondary reactions at the surface can also play a role in regulating the reaction rate[30,31]. A general first order reaction equation is implemented[1],

$$S_s(\vec{r_s}, t) = k(\vec{r_s}) \left(C_c(\vec{r_s}, t) - C_{eq,c} \right), \vec{r_s} \in \Gamma, t > 0, \tag{4}$$

that controls the deposition at the electrode surface and subsequent dendrite surface. The model uses a first order reaction because the reduction reaction depends on the concentration of a single species (Li⁺).

Thus, the boundary condition for cations at the interface is

$$D_c \nabla C_c(\overrightarrow{r_s}, t) + \mu_c C_c(\overrightarrow{r_s}, t) \nabla \phi(\overrightarrow{r_s}, t) = S_s(\overrightarrow{r_s}, t), \overrightarrow{r_s} \in \Gamma, t > 0.$$
 (5)

There is a zero flux boundary condition for anions at the interface[18],

$$D_A \nabla C_A(\vec{r}_s, t) + \mu_A C_A(\vec{r}_s, t) \nabla \phi(\vec{r}_s, t) = 0, \vec{r}_s \in \Gamma, t > 0. \tag{6}$$

The total change in mass in the solid due to interactions with the fluid is given by

$$\frac{\delta m(\vec{r_s}, t)}{\delta t} = k(\vec{r_s}) \left(C_c(\vec{r_s}, t) - C_{eq,c} \right), \vec{r_s} \in \Gamma, t > 0, \tag{7}$$

which balances the change in mass in the fluid domain. The specific mass in the model is used to track the solute concentration in the solid particles and therefore has similar units as the concentration in the fluid particles.

SPH discretization

The governing equations are discretized using the SPH method to simulate diffusion, ionic migration and precipitation at the electrode-electrolyte interface. In SPH simulations, the domain is represented by particles which obey continuum scale mechanics that can be approximated by a linear combination of smoothed kernel functions centered around the particles[24]. Each particle has a set of explicit properties, $\{a\}$, and a resultant scalar field A(r) approximated by

$$A(\mathbf{r}_i) = \sum_{j} \frac{m_j a_j}{\rho_j} W(\overrightarrow{r}_{ij}, h)$$
 (8)

where r_i , m_i and ρ_i are the position, mass and density of particle i, respectively. W is the SPH smoothing function, which is compact and non-zero up to the distance h from particle i. The distance between particle i and j is $\overrightarrow{r_{ij}}$. Similarly, the gradient of the scalar field, ∇A , can be approximated by

$$\nabla A(\mathbf{r}_i) = \sum_{i} \frac{m_i a_j}{\rho_j} \nabla W(\overrightarrow{r_{ij}}, h)$$
(9)

Many forms of the smoothing function with continuous derivatives have been used in SPH modeling. An M_6 smoothing function[32],

$$W(\overrightarrow{r_{ij}}, h) = \alpha \begin{cases} \left(3 - \frac{3|\overrightarrow{r_{ij}}|}{h}\right)^{5} - 6\left(2 - \frac{3|\overrightarrow{r_{ij}}|}{h}\right)^{5} + 15\left(1 - \frac{3|\overrightarrow{r_{ij}}|}{h}\right)^{5} & 0 \le |\overrightarrow{r_{ij}}| < h/3 \\ \left(3 - \frac{3|\overrightarrow{r_{ij}}|}{h}\right)^{5} - 6\left(2 - \frac{3|\overrightarrow{r_{ij}}|}{h}\right)^{5} & h/3 \le |\overrightarrow{r_{ij}}| < 2h/3 \\ \left(3 - \frac{3|\overrightarrow{r_{ij}}|}{h}\right)^{5} & 2h/3 \le |\overrightarrow{r_{ij}}| < h \\ 0 & h < |\overrightarrow{r_{ij}}| \end{cases}$$

is used in this work where $\alpha=\frac{63}{478\pi h^2}$ for two spatial dimensions. $W(\overrightarrow{r_{ij}},h)$ will be denoted as W_{ij} in the following equations.

The SPH model discretizes the computational domain into two sub-domains of particles: Ω_f is discretized with "fluid" particles that make up the electrolyte and Ω_s is discretized with "solid" particles that form the electrode and precipitates. Since there is no convection in the current model, both particle sets do not move but fluid particles can precipitate into solid particles and the solid particles can dissolve into fluid particles as described in Tartakovsky et al[25].

Each fluid particle has a concentration of both anions and cations and a local potential. Building upon the SPH formulation for diffusion by Tartakovsky et al[25], the cation concentration is calculated from the Nernst-Plank equation (Eq. 1) as

$$\frac{DC_{c,i}}{Dt} = \sum_{j \in fluid} \frac{2D_c m_j \overline{r_{ij}}}{\rho_j (\overline{r_{ij}})^2} (C_{c,i} - C_{c,j}) \nabla W_{ij} + \sum_{j \in fluid} \frac{m_j \overline{r_{ij}}}{\rho_j (\overline{r_{ij}})^2} \mu_c (C_{c,i} - C_{c,j}) (\phi_i - \phi_j) \nabla W_{i,j} - S_{V,i}, i \in fluid particles$$
(11)

where the subscript c refers to the cation properties and $C_{c,i}$ describes the cation concentration at position r_i . The SPH-CSR formulation developed by Ryan et al[33] reformulates the heterogeneous boundary condition of Eq. 4 as a homogeneous boundary condition and a volumetric source term, S_v . The volumetric source term is calculated from S_s (Eq. 3), a characteristic function (β), and the surface normal vectors (n_i) as,

$$S_{V,i} = S_s \sum_{\kappa \in solid} \frac{m_k}{\rho_k} (\overrightarrow{n_k} + \overrightarrow{n_i}) (\overrightarrow{\beta_k} + \overrightarrow{\beta_i}) \nabla W_{i,k}$$
 (12)

where the normal vector can be calculated by

$$\overrightarrow{n_i} = \frac{\sum_j \frac{m_j}{\rho_j} (\beta_j - \beta_i) \nabla W_{i,j}}{\left| \sum_j \frac{m_j}{\rho_j} (\beta_j - \beta_i) \nabla W_{i,j} \right|},\tag{13}$$

and β is defined as,

$$\beta_{i} = \begin{cases} \beta_{f} = 0, i \in fluid \ particles \\ \beta_{s} = 1, i \in solid \ particles \end{cases}$$
 (14)

to distinguish the solid and fluid domains.

The anion concentration is discretized as

$$\frac{DC_{a,i}}{Dt} = \sum_{j \in fluid} \frac{2D_a m_j \overrightarrow{r_{ij}}}{\rho_j (\overrightarrow{r_{ij}})^2} (C_{a,i} - C_{a,j}) \nabla W_{i,j} +
\sum_{j \in fluid} \frac{m_j \overrightarrow{r_{ij}}}{\rho_j (\overrightarrow{r_{ij}})^2} (\mu_a C_{a,i} - \mu_a C_{a,j}) (\phi_i - \phi_j) \nabla W_{i,j}, i \in fluid particles.$$
(15)

Where the subscript a refers to anion properties and $C_{a,i}$ describes the anion concentration at position r_i .

The electrostatic potential equation is discretized by

$$\phi_{i} = \frac{e(z_{c,i}C_{c,i} - z_{a,i}C_{a,i})}{\epsilon \epsilon_{0}} + \frac{1}{4\pi\epsilon\epsilon_{0}} \sum_{j \in fluid} \frac{e(z_{c,j}C_{c,j} - z_{a,j}C_{a,j})}{\overrightarrow{r_{ij}}}, i \in fluid \ particles$$
 (16)

where the subscripts i and j refer to particles i and j. The potential at the reactive surface (electrode and dendritic growth) is the reference potential, which is equal to the ground potential,

$$\phi(\vec{r_s}, t) = 0, \vec{r_s} \in \Gamma, t > 0 \tag{17}$$

and the potential at the top boundary outside of the diffusion layer has a fixed potential of ϕ_0 relative to the reference potential,

$$\phi(y = L, t) = \phi_0, t > 0 \tag{18}$$

The potential throughout the fluid domain is calculated using the discretized Poisson equation, Eq. 16.

In the solid particles, diffusion and migration are neglected and the change of mass of the solid balances the loss of ions in the liquid particles,

$$\frac{dm_i}{dt} = k_i \left(C_i - C_{eq} \right) \sum_{\kappa \in solid} \frac{m_k}{\rho_k} (\overrightarrow{n_k} + \overrightarrow{n_l}) (\overrightarrow{\beta_k} + \overrightarrow{\beta_l}) \nabla W_{i,k}. \tag{19}$$

The process of precipitation and dendrite growth is simulated by tracking the mass, m_i , in the solid. When the mass of a particle surpasses twice the initial mass, m_0 , the nearest fluid particle precipitates and becomes a solid. The new solid particle has a mass of m_0 and the original solid particle's mass becomes $(m_i - m_0)$.

The SPH model is implemented into the LAMMPS code base, as part of an SPH module[34]. The simulation domain (Figure 1) is two dimensional and includes 262,144 particles, discretizing a square domain of 128 by 128 units of h (except in the convergence cases) with an average particle density (number of particles within area h^2) of 16. The domain is divided between fluid and solid particles.

Verification and Convergence Studies

While the implementation of the full Nernst-Planck equation has not been previously verified, the implementation of the diffusion and reaction terms have been [26,28]. As such, the verification cases presented here focus on verifying the electrochemical potential and migration equations for two oppositely charged species. Two separate verification cases are presented to assess the accuracy of the implemented mathematical models (i.e.

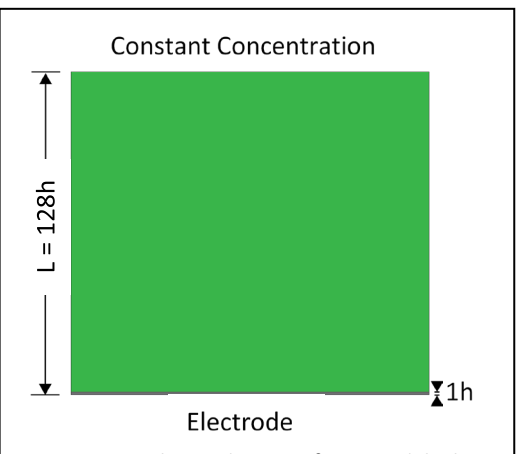


Figure 1. Simulation domain of SPH model. The green region represents the fluid particles (electrolyte) and the grey region represents the solid particles (electrode). A constant concentration boundary layer is 128 kernel lengths away from the electrode.

Eqs. 11-19); the first case considers the cation concentration change due to migration under a constant electric field. While the second case considers the concentration change for both cations and anions due to migration subject to a varying electric field. The electric field is concentration-dependent; it changes due to differences in local concentrations according to Eq. 16. For the second case, an analytical solution does not exist and so a comparison is made to numerical integration of the governing equations using the Runge Kutta method. For both cases, the SPH simulations were conducted in a two dimensional square domain (0 < x < L, 0 < y < L) and the one dimensional concentration through the electrolyte was calculated by dividing L into n bins in the x dimension and then taking the mean of each bin.

Case 1:

The 1-D governing equation of migration under constant electric field is

$$\frac{\partial C}{\partial t} = \mu \mathbf{E} \frac{\partial C}{\partial x} \tag{20}$$

where 0 > x > L = 1 and $\mu E = 1$ and the initial concentration is given as

$$C(x,t=0) = \exp\left[-\frac{1}{2}\left(\frac{(x-\mu_m)}{\sigma}\right)^2\right]$$
 (21)

where μ_m/L is 0.5 and $(\sigma/L)^2$ is 0.01 and the boundary conditions are

$$C(x = 0, t) = c(x = L, t) = 0.$$
 (22)

The analytical solution of Eq. 20 can then be derived as,

$$C(x,t) = \exp\left[-\frac{1}{2}\left(\frac{(x+\mu Et) - \mu_m}{\sigma}\right)^2\right]. \tag{23}$$

Case 2:

In Case 2, the potential is governed by Eq. 2 and the concentration is governed by Eq. 1 with the diffusion coefficient set to zero. The concentrations for the anions and cations are subject to the initial concentration,

$$C_c(x,t=0) = C_a(x,t=0) = \frac{1}{2} \operatorname{erfc}\left(\frac{x-\mu_m}{\sigma\sqrt{2}}\right)$$
 (24)

and the boundary conditions are $C_c(x=0,t)=C_a(x=0,t)=1$ and $C_c(x=L,t)=C_a(x=L,t)=0$. The initial concentration was selected so that the concentration varied smoothly; large disparities in concentration between the two species are non-physical.

For Case 1, both the SPH model and the Runge-Kutta method are compared to the analytical solution and in Case 2 the SPH model is compared to the Runge-Kutta method. As shown in Figure 2, the SPH model compares well to both Cases 1 and 2. The average L1 relative error is less than 0.001 for both cases. The L1 relative error, E_{L1} , is calculated as

$$E_{L1} = \frac{1}{n} \sum_{1}^{n} \frac{|C_{A,i} - C_{B,i}|}{\max(C_{B,i})}$$
 (25)

where $C_{A,i}$ and $C_{B,i}$ are the concentrations predicted at location i for methods A and B over all particles, n. Eq. 25 is used to calculate the L1 relative error between the SPH method, analytical solution and Runge-Kutta numerical integrator.

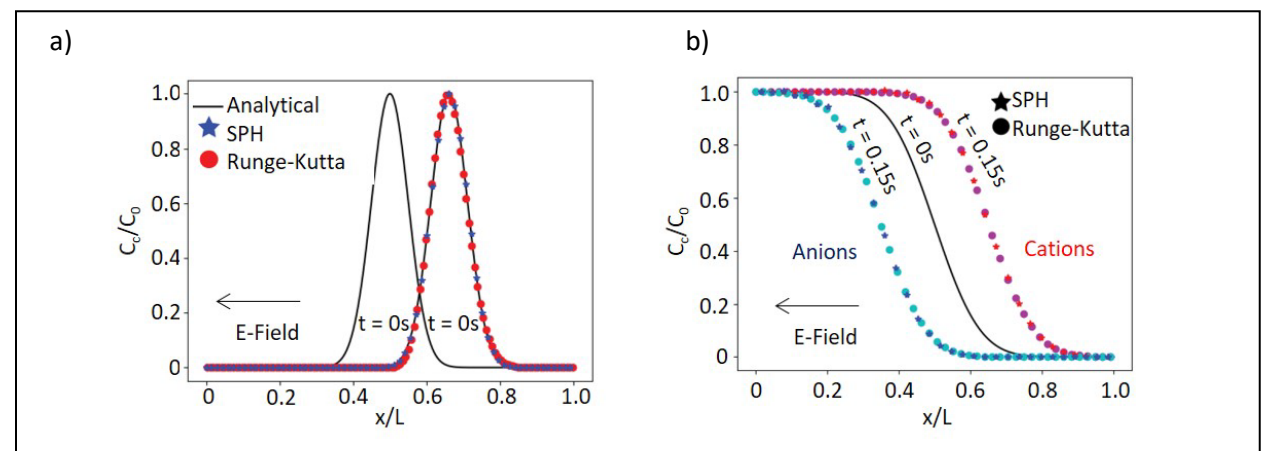


Figure 2. (a) Concentration profile for test Case 1 where the migration is driven by a constant electric field and compares the results of the analytical solution, the SPH model and the Runge-Kutta method with an L1 average error of less than 1%. (b) Concentration profile for test Case 2 where the migration is calculated for both the concentrations of anions and cations and is driven by a concentration-dependent electric field.

The effects of particle ordering on the SPH results were also considered. In both Cases 1 and 2, the SPH simulations were completed using particles placed with equal, ordered spacing. To consider the effects of disordered particles, Case 2 was also run with randomly spaced particles. The particles are disordered by

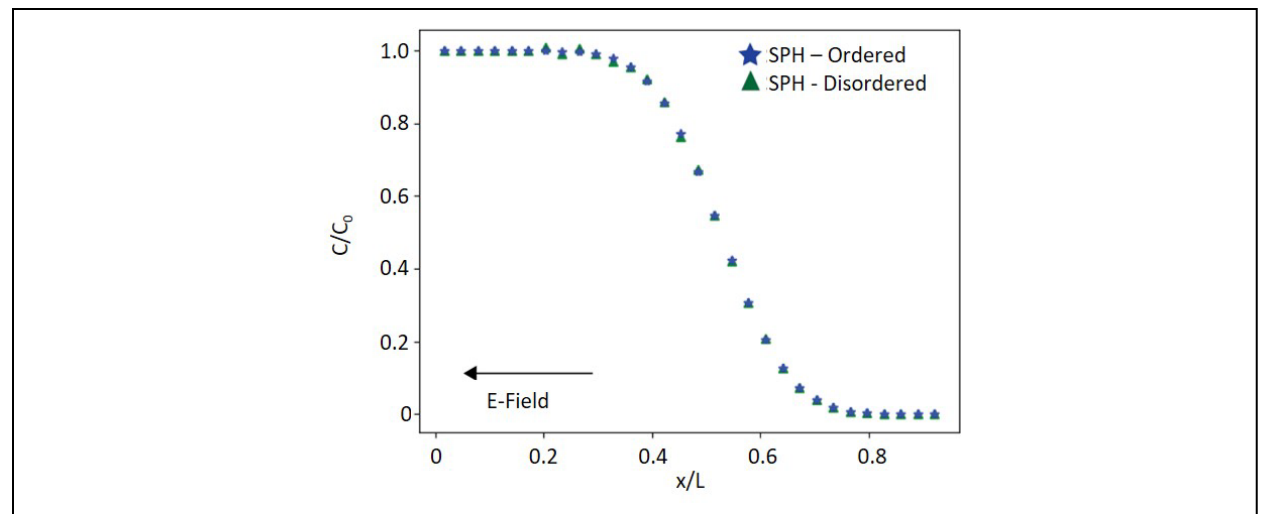


Figure 3. Concentration profile for the ordered and disordered particle placement of SPH simulations for Case 2 with 0.12% L1 relative error. This comparison was made to demonstrate the model's ability to arrive at similar concentration levels regardless of SPH particle positioning. This is what allows SPH to accurately model the morphological evolution of dendritic growths.

shifting them randomly up to a maximum of 20% of their initial spacing. As seen in Figure 3, the ordered particle SPH simulation and the disordered particle SPH simulation compare well with a maximum difference between the ordered and disordered simulations of less than 0.11%.

Additionally, the effects of spatial resolution are compared for the SPH simulation of Case 2 in terms of both the error and the computational cost. Figure 4 depicts the L1 error of the SPH simulations compared to the numerical integrator at different spatial resolutions as well as the time for the simulation to run

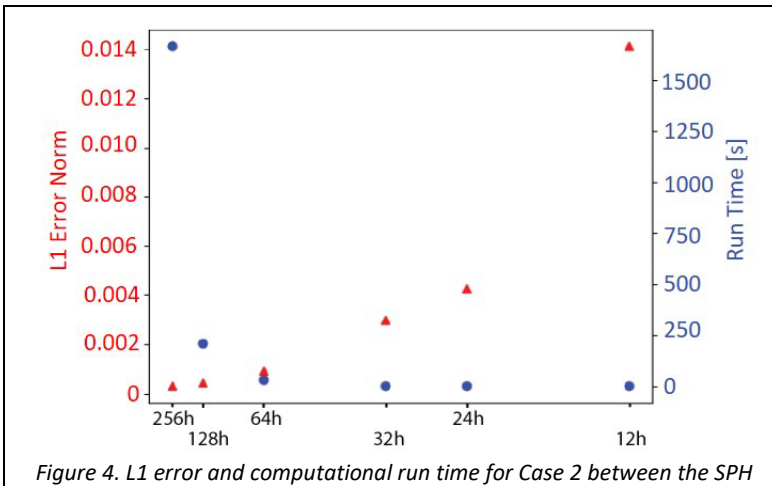


Figure 4. L1 error and computational run time for Case 2 between the SPH simulation and the Runge-Kutta numerical integrator method at different particle spacing in the SPH model. Simulations use a particle spacing of 128h because of the high density and low run time.

~1.3 million time steps. Based on the relative low error and fast run time, L=128h was chosen for the particle spacing.

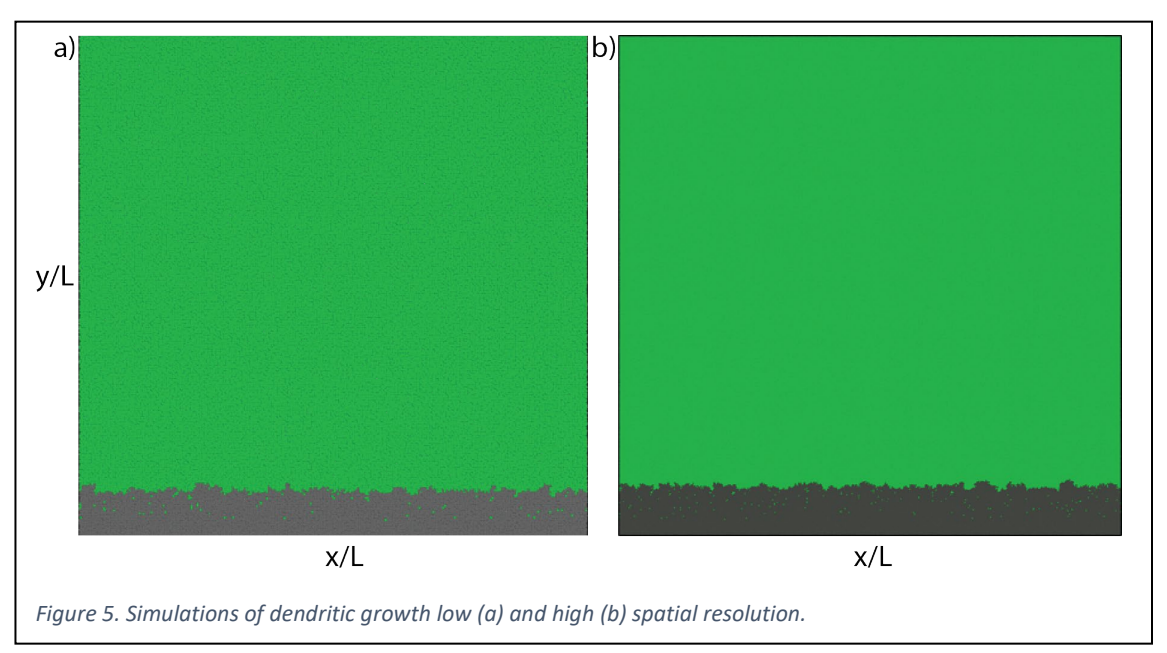
A dendritic growth convergence study was conducted to demonstrate the model's ability to accurately simulate dendritic growth. In Figure 5, simulations are presented at differing resolutions (Figure 5a: *L*=64h and 65,536 particles, Figure 5b: *L*=128h and 262,144 particles).

The average growth fronts of the low- and high-resolution simulations were compared in Figure 6. The

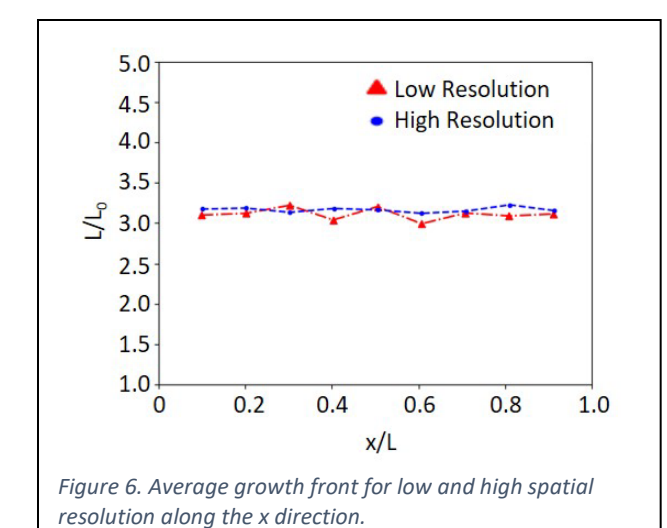
average growth fronts were calculated using bin averaging in the x-dimension. The simulations at the two resolutions predict similar average growth fronts with less than 5% relative difference (Figure 7).

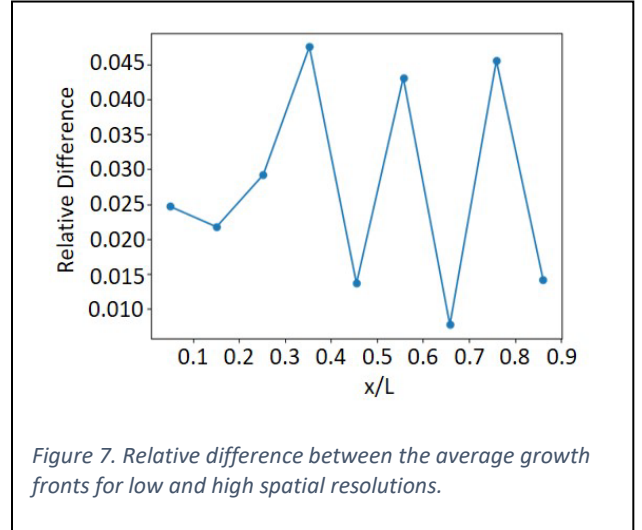
Application to Dendritic growth in Electrodeposition

As mentioned previously, non-uniform deposition can lead to dendritic growth, which is problematic in a variety of electrodeposition processes where precision is required. To further evaluate the SPH model's ability to capture dendritic growth and morphology, the SPH model was used to simulate experimental data of dendrite growth under high and low current scenarios and under pulsed plating conditions.



Experimental data from Schneider et al[35] on electrodeposition of copper under galvanostatic conditions under various growth rates and pulsed plating conditions are used for comparison to the SPH model. The growth front lengths are plotted based on the experimental imaging (Figure 8b). The growth front length is a normalized length, to measure surface roughness. It is normalized by the length for a smooth surface





such that a smoother deposition will have a value close to 1 and dendritic growth will have a value higher than 1.

The first two experimental tests are conducted at a lower and higher growth rate. In the experimental work the higher growth rate condition used an applied current that was five times higher than that of the lower growth rate condition. These were conducted to provide baseline evidence for different electrodeposition regimes where the lower growth rate from lower applied current produces reaction rate limited conditions and relatively uniform electrodeposition (Figure 8a, top), and the higher growth rate from higher applied current produces mass transport limited conditions and high dendritic growth (Figure 8b, bottom).

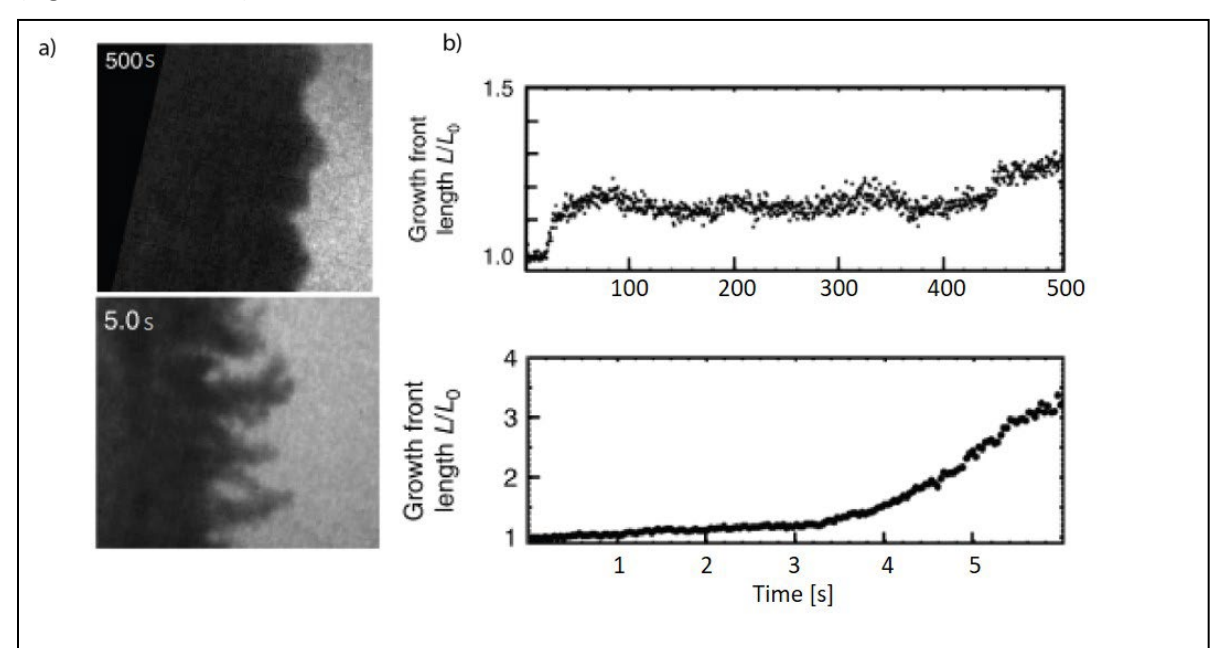


Figure 8. Experimental observations of dendritic growth. (a) Images of dendrites under low growth rate (top) and high growth rate (bottom). Note the values in upper left corner of images are the experimental time. (b) Measurements of the dendritic growth front over time for the low and high growth rates. Image from Schneider et al[30] is licensed under creativecommons.org/licenses/by/4.0/.

At lower growth rates (Figure 8, top), the deposition is relatively uniform along the electrode surface as demonstrated by the normalized growth front length close to 1. The growth front moves in unison suggesting the system is reaction rate limited and the local current density is also relatively uniform. At higher growth rates (Figure 8, bottom), the applied current is increased 5x higher than the low growth rate conditions. The ionic deposition forms dendrites suggesting mass transport limited conditions. Under the high growth rate, the deposition morphology is a long, thin branching structure. There is rapid growth at the tips of the dendrites and hardly any deposition in the regions without dendrites. The normalized growth front length (Figure 8b, bottom) increases rapidly once there are mass transport limited condition for the reaction at the anode.

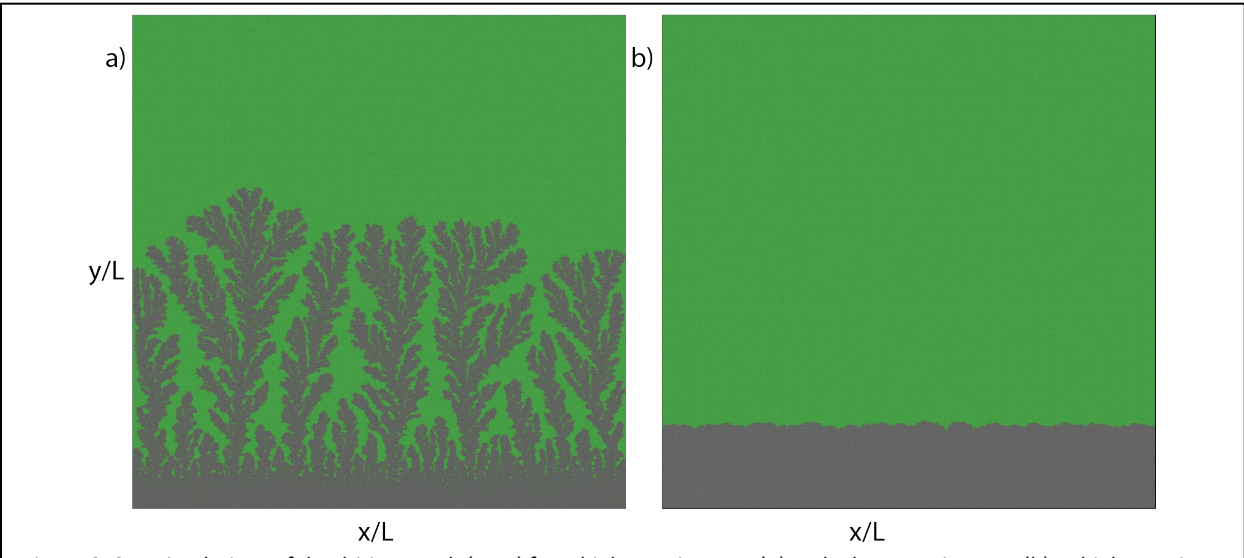
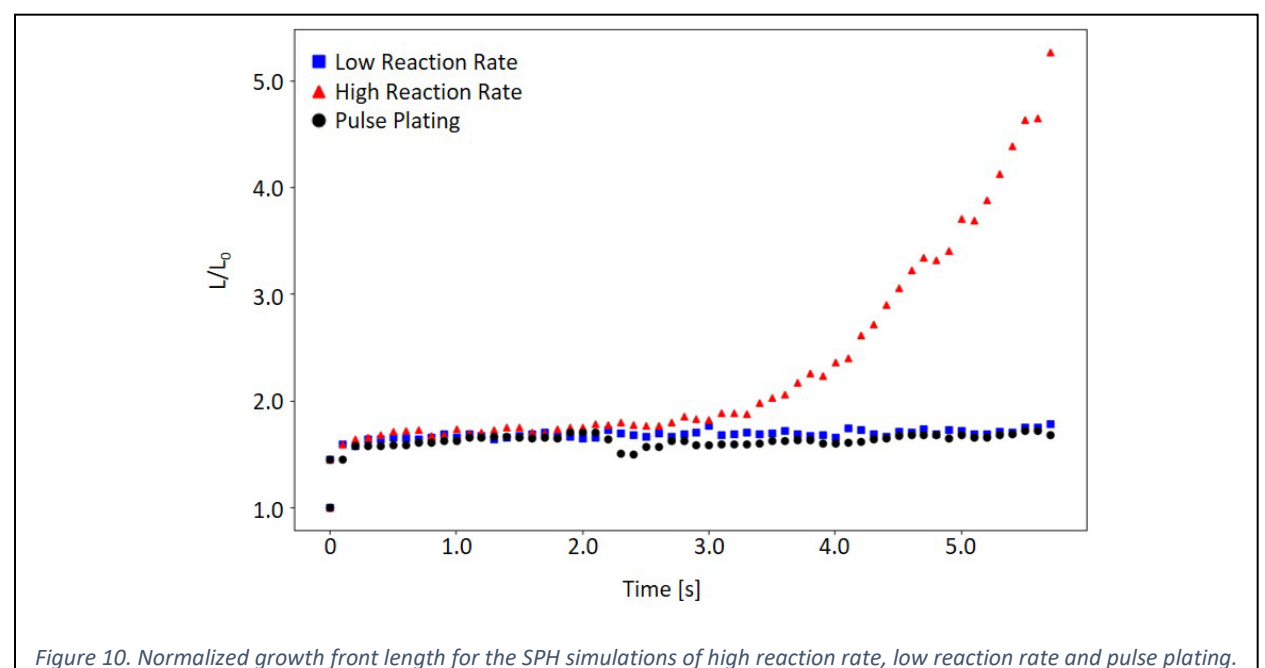


Figure 9. SPH simulations of dendritic growth (grey) for a high reaction rate (a) and a low reaction rate (b). A high reaction rate condition – also known as diffusion limited condition – favors dendritic morphologies due to precipitation being more likely to occur away from the surface where there are higher ion concentrations creating more elongated structures. Whereas the low reaction rate condition – also known as reaction rate limited condition – has a more uniform deposition morphology as ion transport to the surface replenishes deposited ions.

The SPH model is able to capture similar dendritic behavior. The reaction rate is the model parameter that is comparable to the applied current in the experimental tests. Initially, there is a 1 h thick layer of solid particles at y=0 and the rest of the domain is fluid particles. The concentration at y=L is held constant throughout the simulations to represent the concentration outside of the diffusion layer, which is a common assumption in modeling electrochemical systems, and has been shown to accurately represent the physical system[1,36]. In Figure 9, a simulation of dendritic growth (grey) is presented at a high (a) and low (b) reaction rate. The high reaction rate is five times higher than the lower reaction rate, matching the conditions in the experimental tests. Long, thin dendritic branching occurs in the high reaction rate case and a more uniform deposition occurs at the lower reaction rate.

The normalized growth front length at different times is shown in Figure 10. The curves for the low and high reaction rate simulations compare well with the trends of the growth front curves from the experimental tests. At the low reaction rate, the normalized growth front length remains between 1 and 2 indicating uniform deposition but at the higher reaction rate, the growth front length increases exponentially as expected when there are long dendrite growths and regions without growth.

Schnieder et al also conducted experiments on the effects of pulse plating on dendrite growth (Figure 11). Pulse plating has been suggested as a method for rapidly charging batteries while concurrently maintaining smoother deposition[37]. Schneider et al conducted experimental tests using the high growth rate of Figure 8 for 1 s followed by a 5 s rest period, allowing the ionic concentration near the interface to equilibrate. The SPH model was also used to test pulse plating with a matching high reaction rate to rest period ratio. As demonstrated by both the experimental data and SPH simulations, pulse plating allows the deposition to occur more uniformly along the electrode surface resulting in a smaller normalized growth front length, Figure 10. Note that the experiments by Schnieder et al [37] focused on surface roughness and plating in electrochemical deposition on a copper plate and did not consider battery applications. In recent work, we have expanded these initial pulse plating studies to consider pulse plating effects for fast charging of batteries[38].



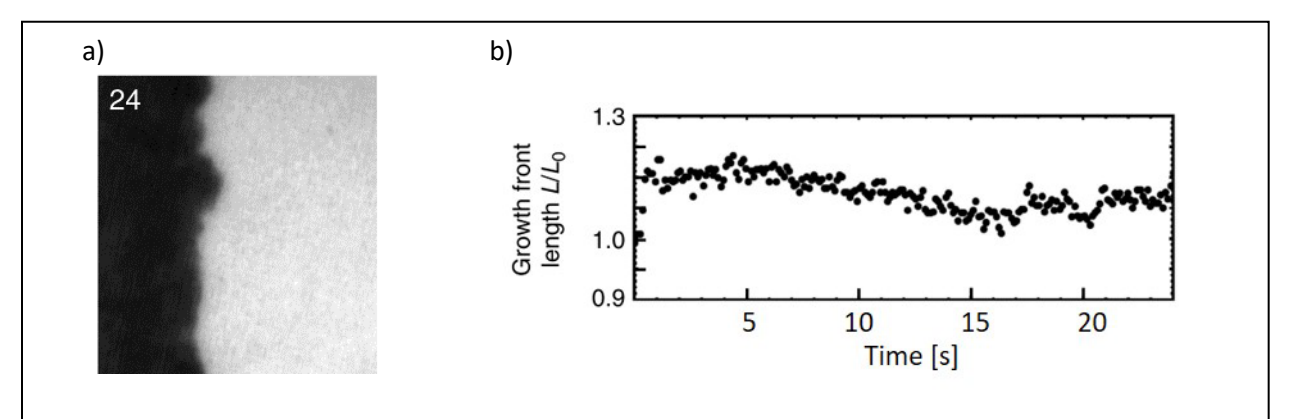


Figure 11. Experimental observations (a) and normalized growth front length (b) of dendrite growth under pulse plating conditions. Image from Schneider et al[30] is licensed under creativecommons.org/licenses/by/4.0/.

Conclusion

Electrodeposition is used in a variety of industrial applications and is critical to the fabrication of electronics and the performance of batteries. Experimentally observing the electrodeposition process *in situ* at the electrolyte-electrode interface is challenging. However, computational models are able to isolate this region to understand the critical phenomena occurring at the interface during electrodeposition. With this understanding, the electrodeposition process can be better controlled leading to improved deposition in fabrication processes, and improved performance in battery applications.

A numerical model based on the SPH method was presented for simulating mass transport and electrodeposition near an interface. The Nernst-Planck equations were implemented in the model to track concentration changes of two oppositely charged species due to diffusion and ionic migration. The Poisson equation is solved to calculate the local potential throughout the domain. The expanded physics of the SPH model presented here allows more accurate modeling of the physical processes at the interface then previous SPH models that did not include electric field effects, and is better able to simulate experimental conditions. The implementation of the Nernst-Planck equation was verified with an analytical solution and a numerical integration method. The SPH model was shown to accurately reproduce the verification cases.

Dendritic morphology predicted by the SPH model qualitatively matches experimental data for both low and high reaction rate scenarios. Additionally, the growth front length of the dendrites predicted by SPH agree with experimental data and show that for the high reaction rate the growth front increases exponentially, while the growth front length is stable for the low reaction rate. Pulse plating simulations were also presented as a viable technique for reducing dendritic growth. The SPH model accurately captures the behavior of ionic deposition for pulsed plating and predicts a growth front comparable to the experimental data. Further work on pulsed plating for fast charging applications, and current-voltage relations with the SPH model have been considered and are presented in Morey et al[39], and Melsheimer et al[38].

Explicitly tracking conditions, i.e. concentration and potential, near the electrode-electrolyte interface can lend insight into advanced methods for controlling the deposition morphology, such as structured electrolytes[40,41], novel separator designs[42–44], and surface treatments[39,45]. The results of the computational studies demonstrate the model's ability to capture the complex interfacial physics occurring during the electrodeposition process. Additionally, the model could be used to understand the

mechanical effects of dendrite growth in non-liquid electrolytes with the addition of solid mechanics equations, which have been used in SPH modeling of other multiphase systems for biological and geological applications[46–48].

Acknowledgements

Financial support for this research is provided by the National Science Foundation through award numbers 1911698, 1727316, and 2034154.

Data availability

The raw data required to reproduce these findings are available via email request to the corresponding author.

References

- [1] J. Newman, K.E. Thomas-Alyea, Electrochemical systems, 3rd ed., John Wiley & Sons, Inc., 2012.
- [2] J.E.B. Randles, Kinetics of rapid electrode reactions, Faraday Discuss. (1947). https://doi.org/10.1039/DF9470100011.
- [3] R.F. Voss, M. Tomkiewicz, Computer Simulation of Dendritic Electrodeposition, J. Electrochem. Soc. (1985). https://doi.org/10.1149/1.2113841.
- [4] L. Barchi, U. Bardi, S. Caporali, M. Fantini, A. Scrivani, A. Scrivani, Electroplated bright aluminium coatings for anticorrosion and decorative purposes, Prog. Org. Coatings. 67 (2010) 146–151. https://doi.org/10.1016/j.porgcoat.2009.10.017.
- [5] F.H. Hurley, T.P. Wler, The Electrodeposition of Aluminum from Nonaqueous Solutions at Room Temperature, J. Electrochem. Soc. 98 (1951) 207. https://doi.org/10.1149/1.2778133.
- [6] N. Jiang, B. You, M. Sheng, Y. Sun, Electrodeposited Cobalt-Phosphorous-Derived Films as Competent Bifunctional Catalysts for Overall Water Splitting, Angew. Chemie. 127 (2015) 6349–6352. https://doi.org/10.1002/ange.201501616.
- [7] H. Kim, N.P. Subramanian, B.N. Popov, Preparation of PEM fuel cell electrodes using pulse electrodeposition, J. Power Sources. 138 (2004) 14–24. https://doi.org/10.1016/j.jpowsour.2004.06.012.
- [8] L. Frenck, G.K. Sethi, J.A. Maslyn, N.P. Balsara, Factors That Control the Formation of Dendrites and Other Morphologies on Lithium Metal Anodes, Front. Energy Res. (2019). https://doi.org/10.3389/fenrg.2019.00115.
- [9] K.N. Wood, M. Noked, N.P. Dasgupta, Lithium metal anodes: Toward an improved understanding of coupled morphological, electrochemical, and mechanical behavior, ACS Energy Lett. (2017). https://doi.org/10.1021/acsenergylett.6b00650.
- [10] J. Wang, B. Ge, H. Li, M. Yang, J. Wang, D. Liu, C. Fernandez, X. Chen, Q. Peng, Challenges and progresses of lithium-metal batteries, Chem. Eng. J. 420 (2021) 129739. https://doi.org/https://doi.org/10.1016/j.cej.2021.129739.

- [11] M. Rosso, T. Gobron, C. Brissot, J.N. Chazalviel, S. Lascaud, Onset of dendritic growth in lithium/polymer cells, in: J. Power Sources, 2001. https://doi.org/10.1016/S0378-7753(01)00734-0.
- [12] L. AVRAMOVIĆ, E.R. IVANOVIĆ, V.M. MAKSIMOVIĆ, M.M. PAVLOVIĆ, M. VUKOVIĆ, J.S. STEVANOVIĆ, N.D. NIKOLIĆ, Correlation between crystal structure and morphology of potentiostatically electrodeposited silver dendritic nanostructures, Trans. Nonferrous Met. Soc. China (English Ed. 28 (2018) 1903–1912. https://doi.org/10.1016/S1003-6326(18)64835-6.
- [13] X. Zhang, Y. Yang, Z. Zhou, Towards practical lithium-metal anodes, Chem. Soc. Rev. 49 (2020) 3040–3071. https://doi.org/10.1039/c9cs00838a.
- [14] E.M. Ryan, P.P. Mukherjee, Mesoscale modeling in electrochemical devices—A critical perspective, Prog. Energy Combust. Sci. 71 (2019) 118–142. https://doi.org/10.1016/J.PECS.2018.11.002.
- [15] A. Wang, S. Kadam, H. Li, S. Shi, Y. Qi, Review on modeling of the anode solid electrolyte interphase (SEI) for lithium-ion batteries, Npj Comput. Mater. 4 (2018) 15. https://doi.org/10.1038/s41524-018-0064-0.
- [16] N. Moelans, B. Blanpain, P. Wollants, An introduction to phase-field modeling of microstructure evolution, Calphad Comput. Coupling Phase Diagrams Thermochem. (2008). https://doi.org/10.1016/j.calphad.2007.11.003.
- [17] C. Brissot, M. Rosso, J.N. Chazalviel, S. Lascaud, Dendritic growth mechanisms in lithium/polymer cells, J. Power Sources. 81 (1999). https://www.sciencedirect.com/science/article/abs/pii/S0378775398002420.
- [18] J.N. Chazalviel, Electrochemical Aspects of the Generation of Ramified Metallic Electrodeposition, Phys. Rev. A. 42 (1990) 7355–7367.
- [19] X. Guan, A. Wang, S. Liu, G. Li, F. Liang, Y.W. Yang, X. Liu, J. Luo, Controlling Nucleation in Lithium Metal Anodes, Small. (2018). https://doi.org/10.1002/smll.201801423.
- [20] J. Jeon, G.H. Yoon, T. Vegge, J.H. Chang, Phase-Field Investigation of Lithium Electrodeposition at Different Applied Overpotentials and Operating Temperatures, ACS Appl. Mater. Interfaces. 14 (2022) 15275–15286. https://doi.org/10.1021/acsami.2c00900.
- [21] H. Jing, H. Xing, X. Dong, Y. Han, Nonlinear Phase-Field Modeling of Lithium Dendritic Growth during Electrodeposition, J. Electrochem. Soc. 169 (2022) 32511. https://doi.org/10.1149/1945-7111/ac5fed.
- [22] Y. Ren, Y. Zhou, Y. Cao, Inhibit of Lithium Dendrite Growth in Solid Composite Electrolyte by Phase-Field Modeling, J. Phys. Chem. C. 124 (2020) 12195–12204. https://doi.org/10.1021/acs.jpcc.0c01116.
- [23] C.-H. Chen, C.-W. Pao, Phase-field study of dendritic morphology in lithium metal batteries, J. Power Sources. 484 (2021) 229203. https://doi.org/https://doi.org/10.1016/j.jpowsour.2020.229203.
- [24] J.J. Monaghan, Smoothed Particle Hydrodynamics, Reports Prog. Phys. 68 (2005) 1703–1759.
- [25] A.M. Tartakovsky, P. Meakin, T.D. Scheibe, R.M. Eichler West, R.M.E. West, Simulations of

- reactive transport and precipitation with smoothed particle hydrodynamics, J. Comput. Phys. 222 (2007) 654–672. https://doi.org/10.1016/j.jcp.2006.08.013.
- [26] J. Tan, E.M. Ryan, Computational study of electro-convection effects on dendrite growth in batteries, J. Power Sources. 323 (2016) 67–77. https://doi.org/10.1016/j.jpowsour.2016.05.012.
- [27] J. Tan, E.M. Ryan, Numerical modeling of dendrite growth in a lithium air battery system, ECS Trans. 53 (2013) 35–43.
- [28] J. Tan, A. Cannon, E. Ryan, Simulating dendrite growth in lithium batteries under cycling conditions, J. Power Sources. 463 (2020) 228187. https://doi.org/https://doi.org/10.1016/j.jpowsour.2020.228187.
- [29] A. Cannon, E.M. Ryan, Characterizing the Microstructure of Separators in Lithium Batteries and Their Effects on Dendritic Growth, ACS Appl. Energy Mater. (2021). https://doi.org/10.1021/acsaem.1c00144.
- [30] M. Nojabaee, K. Küster, U. Starke, J. Popovic, J. Maier, Solid Electrolyte Interphase Evolution on Lithium Metal in Contact with Glyme-Based Electrolytes, Small. 16 (2020) 1–5. https://doi.org/10.1002/smll.202000756.
- [31] I. Yoon, S. Jurng, D.P. Abraham, B.L. Lucht, P.R. Guduru, Measurement of mechanical and fracture properties of solid electrolyte interphase on lithium metal anodes in lithium ion batteries, Energy Storage Mater. 25 (2020) 296–304. https://doi.org/10.1016/j.ensm.2019.10.009.
- [32] I.J. Schoenberg, Contributions to the Problem of Approximation of Equidistant Data by Analytic Functions, I. J. Schoenb. Sel. Pap. (1988) 58–87. https://doi.org/10.1007/978-1-4899-0433-1_2.
- [33] E.M. Ryan, A.M. Tartakovsky, C. Amon, A Novel Method for Modeling Neumann and Robin Boundary Conditions in Smoothed Particle Hydrodynamics, Comput. Phys. Commun. 181 (2010) 2008–2023. https://doi.org/doi:10.1016/j.cpc.2010.08.022.
- [34] S. Plimpton, LAMMPS, J. Comput. Phys. (1995).
- [35] N.M. Schneider, J.H. Park, J.M. Grogan, D.A. Steingart, H.H. Bau, F.M. Ross, Nanoscale evolution of interface morphology during electrodeposition, Nat. Commun. 8 (2017) 1–10. https://doi.org/10.1038/s41467-017-02364-9.
- [36] E. Khoo, H. Zhao, M.Z. Bazant, Linear Stability Analysis of Transient Electrodeposition in Charged Porous Media: Suppression of Dendritic Growth by Surface Conduction, J. Electrochem. Soc. 166 (2019) A2280--A2299. https://doi.org/10.1149/2.1521910jes.
- [37] H. Yang, E.O. Fey, B.D. Trimm, N. Dimitrov, M.S. Whittingham, Effects of Pulse Plating on lithium electrodeposition, morphology and cycling efficiency, J. Power Sources. 272 (2014) 900–908. https://doi.org/https://doi.org/10.1016/j.jpowsour.2014.09.026.
- [38] T. Melsheimer, M. Morey, A. Cannon, E.M. Ryan, Modeling the Effects of Pulse Plating on Dendrite Growth in Lithium Metal Batteries, Electrochem. Acta. (n.d.).
- [39] M. Morey, J. Loftus, A. Cannon, E. Ryan, Interfacial studies on the effects of patterned anodes for guided lithium deposition in lithium metal batteries, J. Chem. Phys. 156 (2021) 14703. https://doi.org/10.1063/5.0073358.
- [40] D. Sharon, P. Bennington, S.N. Patel, P.F. Nealey, Stabilizing Dendritic Electrodeposition by

- Limiting Spatial Dimensions in Nanostructured Electrolytes, ACS Energy Lett. 5 (2020) 2889–2896. https://doi.org/10.1021/acsenergylett.0c01543.
- [41] S. Rajendran, Z. Tang, A. George, A. Cannon, C. Neumann, A. Sawas, E. Ryan, A. Turchanin, L.M.R. Arava, Inhibition of Lithium Dendrite Formation in Lithium Metal Batteries via Regulated Cation Transport through Ultrathin Sub-Nanometer Porous Carbon Nanomembranes (Adv. Energy Mater. 29/2021), Adv. Energy Mater. 11 (2021) 2170114. https://doi.org/https://doi.org/10.1002/aenm.202100666.
- [42] C. Li, S. Liu, C. Shi, G. Liang, Z. Lu, R. Fu, D. Wu, Two-dimensional molecular brush-functionalized porous bilayer composite separators toward ultrastable high-current density lithium metal anodes, Nat. Commun. 10 (2019) 1363. https://doi.org/10.1038/s41467-019-09211-z.
- [43] S. Gao, A. Cannon, F. Sun, Y. Pan, D. Yang, S. Ge, N. Liu, A.P. Sokolov, E. Ryan, H. Yang, P.-F. Cao, Glass-fiber-reinforced polymeric film as an efficient protecting layer for stable Li metal electrodes, Cell Reports Phys. Sci. (2021) 100534. https://doi.org/https://doi.org/10.1016/j.xcrp.2021.100534.
- [44] N. Li, W. Wei, K. Xie, J. Tan, L. Zhang, X. Luo, K. Yuan, Q. Song, H. Li, C. Shen, E.M. Ryan, L. Liu, B. Wei, Suppressing Dendritic Lithium Formation Using Porous Media in Lithium Metal-Based Batteries, Nano Lett. (2018). https://doi.org/10.1021/acs.nanolett.8b00183.
- [45] R. Pathak, K. Chen, A. Gurung, K.M. Reza, B. Bahrami, J. Pokharel, A. Baniya, W. He, F. Wu, Y. Zhou, K. Xu, Q.Q. Qiao, Fluorinated hybrid solid-electrolyte-interphase for dendrite-free lithium deposition, Nat. Commun. 11 (2020) 93. https://doi.org/10.1038/s41467-019-13774-2.
- [46] M. Toma, R. Chan-Akeley, J. Arias, G. Kurgansky, W. Mao, Fluid–Structure Interaction Analyses of Biological Systems Using Smoothed-Particle Hydrodynamics, Biology (Basel). 10 (2021). https://doi.org/10.3390/biology10030185.
- [47] C. Peng, X. Guo, W. Wu, Y. Wang, Unified modelling of granular media with Smoothed Particle Hydrodynamics, Acta Geotech. 11 (2016) 1231–1247. https://doi.org/10.1007/s11440-016-0496-y.
- [48] X. Zhou, W.-W. Yao, F. Berto, Smoothed peridynamics for the extremely large deformation and cracking problems: Unification of peridynamics and smoothed particle hydrodynamics, Fatigue Fract. Eng. Mater. Struct. 44 (2021) 2444–2461. https://doi.org/https://doi.org/10.1111/ffe.13523.